Research article

Hydrogen bond-mediated self-assembly of Tin (II) oxide wrapped with Chitosan/[BzPy]Cl network: An effective bionanocomposite for textile wastewater remediation

Mohammad Hossein Arshia [a,b], Ashraf S. Shahvelayati [a,b,*], Shabnam Sheshmani [a,b], Leila Hajiaghababaei [a,b], Mohammad Reza Allahgholi Ghasri [a,b]

[a] *Department of Chemistry, College of Basic Sciences, Yadegar-e- Imam Khomeini (RAH) Shahre Rey Branch, Islamic Azad University, Tehran, Iran*
[b] *Research Center for New Technologies in Chemistry and Related Sciences, Yadegar-e-Imam Khomeini (RAH) Shahre Rey Branch, Islamic Azad University, Tehran, Iran*

A B S T R A C T

A novel and efficient bionanocomposite was synthesized by incorporating SnO into chitosan (Ch) and a room-temperature ionic liquid (RTIL). The bionanocomposite was synthesized in benzoyl pyridinium chloride [BzPy]Cl to maintain the unique properties of SnO, chitosan, and the ionic liquid. Adsorption and photodegradation processes were applied to evaluate the bionanocomposite for removing azo and anthraquinone dyes and textile wastewater. SnO/[BzPy]Cl and SnO/[BzPy]Cl/Ch samples were prepared and characterized using various techniques, including FT-IR, SEM, XRD, EDAX, XPS, DSC, TGA, nitrogen adsorption/desorption isotherm, and DRS analysis. SEM analysis revealed a hierarchical roughened rose flower-like morphology for the biocomposite. The band gap energies of SnO/[BzPy]Cl and SnO/[BzPy]Cl/chitosan were found to be 3.9 and 3.3 eV, respectively, indicating a reduction in the band gap energy with the introduction of [BzPy]Cl and chitosan. SnO/[BzPy]Cl/Ch showed high removal rates (92–95 %) for Fast Red, Blue 15, Red 120, Blue 94, Yellow 160, and Acid Orange 7 dyes. The adsorption kinetics followed a pseudo-second-order model.

In addition, the effect of different photodegradation parameters such as solution pH, dye concentrations, contact time, and amount of photocatalyst, was studied. Given the optimal results obtained in removing azo and anthraquinone dyes, the SnO/[BzPy]Cl/Ch nanocomposite was used as an efficient nanocomposite for removing dyes from textile wastewater. The highest removal efficiency was found to be 95.8 %, obtained under ultraviolet and visible light. Furthermore, BOD and COD reduction analysis showed significant reductions, indicating the excellent performance of the photocatalyst.

1. Introduction

Recently, hybrid nanocomposite materials containing natural polymers like chitosan have been considered to remove dyes from wastewater. The main advantages of these materials are their high availability, easier operation, unique structure, antimicrobial

activity, high efficiency, and low toxicity with hydroxyl and amine functional groups as active adsorption sites. In this respect, some efforts have been made to modify chitosan's chemical and structural properties via different processes through functionalizing and immobilizing with nanostructure metal oxides and ionic liquids. The results can be used to enhance performance, increase surface area, recovery, reusability, and prevent aggregation [1].

During the past few decades, semiconductor metal oxides have been studied for electronic and optoelectronic applications [2]. Tin oxide is one of the important semiconductor metal oxides used for this purpose. Stannic oxide (SnO_2) and stannous oxide (SnO) are the most common members of tine oxides. The oxidation states of +2 and + 4 are responsible for the existence of these two oxides. A wide band gap semiconductor exists in both of these oxides. Several applications of tin (IV) oxide (i.e., SnO2) have been studied, including gas sensors, solar cells, transparent electrodes, and optoelectronics [3]. In contrast, SnO has been used as an anode material [4], coating material [5], photocatalyst [6], and as a precursor for SnO_2 production [7]. SnO is a p-type semiconducting material that can be further enhanced in terms of its band gap value through doping, making it a promising candidate for p-type semiconductor applications. The band gap of metal oxides is influenced by several factors, such as crystal structure, chemical composition, size and shape, temperature, and pressure. In addition, crystal structure affects the band gap by determining the electronic properties of the material, while the chemical composition can alter the band gap width by introducing additional energy levels. As the size of the particle decreases, the band gap tends to increase due to the quantum confinement effect [8].

Ionogel is a term that refers to hybrid nanomaterials that comprise immobilized ionic liquids (ILs) within an inorganic or polymeric matrix. These materials exhibit unique properties, such as high chemical, thermal, and electrochemical stability, superior ionic conductivity, and low vapor pressure. These unique features are attributed to their ionic liquid component and the physicochemical properties of the polymeric matrix host network properties [9]. One of their application is the discharge of colored wastewater from industries such as textile, plastic, leather, pulp mills, and dyestuff manufacturing [10,11].

Nowadays, dye removal using nanotechnology has been developed for different nanostructures, such as zeolites, MCM-41, SBA-15, and hybrid nanocomposites, including ionogels [12].

Nanocomposites' chemical and physical properties in the water treatment were improved by immobilizing some heterogeneous nanostructures such as TiO_2, carbon nanotubes, ZnO, and Fe_3O_4 on the polymeric structure. Thus, designing a new photocatalyst supported by polymeric materials has been the subject of intense research [13].

SnO/[BzPy]Cl/Ch nanocomposite was synthesized as part of our ongoing process for designing novel catalysts capable of both adsorption and degradation in dye wastewater [14]. To this end, we employed [BzPy]Cl ionic liquid and chitosan as a supporting matrix for the synthesized photocatalyst. This matrix allowed for interactions between the functional groups of benzoyl pyridinium chloride and the chitosan, leading to significant enhancements in the photocatalytic properties of the nanocomposite. The results
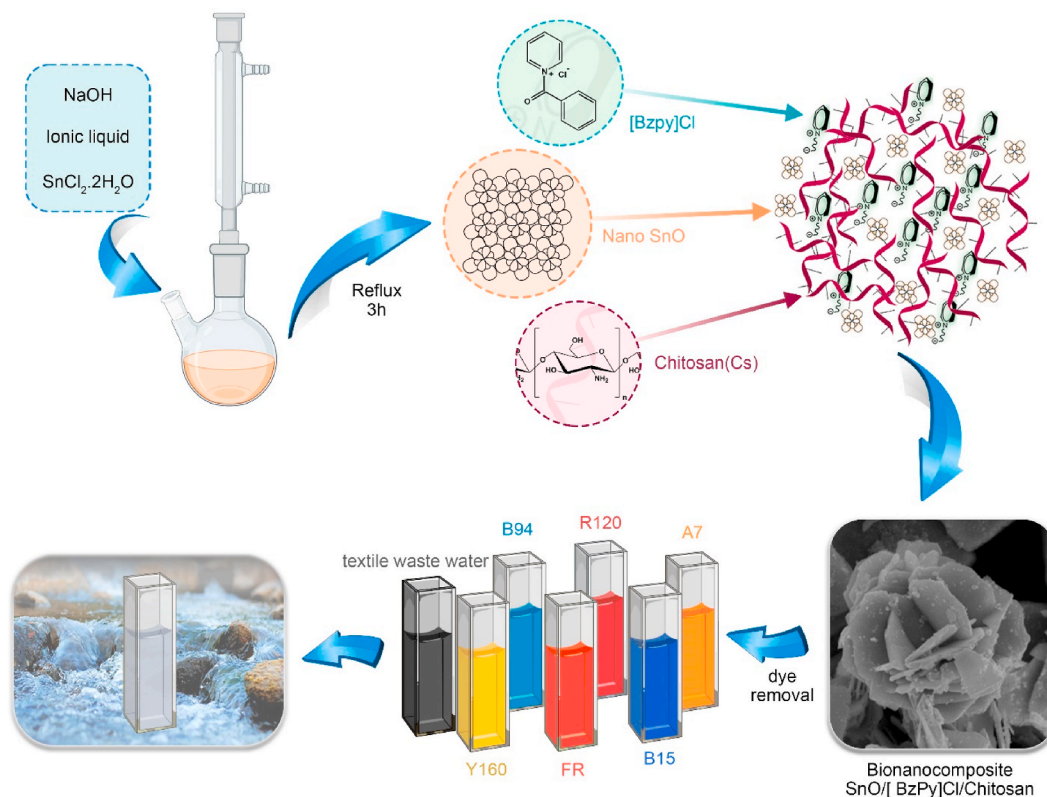

Fig. 1. Preparation of SnO/[BzPy]Cl/Ch bionanocomposite.

showed that this synthesis technique improved the band gap value. In addition, our strategy was further enhanced using SnO/[BzPy]Cl/Ch nanocomposite for the adsorption and degradation of anionic dyes, including azo and anthraquinone dyes. Afterward, it was used for the removal of dye pollutants from textile wastewater an efficient nanocomposite (Fig. 1.). The industrial potential of the SnO/[BzPy]Cl/Ch nanocomposite is highly promising, owing to its exceptional efficiency and simplicity in preparation. Furthermore, it has remarkable effectiveness, reusability, and superior adsorption and photocatalytic capacity.

2. Experimental section

2.1. Materials and physical measurements

All reagents and solvents were purchased commercially and used without further purification. The dyes of analytical purity were purchased from Nordex International, D.Z.E Dye Company in the UK (Fig. S1). FT-IR spectra were obtained using a Thermo/Nicolet Avatar 360 spectrometer (Made in the USA). ^{1}H NMR spectra (300 MHz) were recorded with a Bruker AVANCE 300 MHz in CDCl$_3$. The chemical shift (δ) and coupling constants (J) are reported in ppm and Hz, respectively. The particle morphology and quality elemental analysis of nanocatalysts were investigated by a scanning electron microscope (SEM) and energy dispersive X-ray (EDX), respectively (FESEM, MIRA III TESCAN made in the Czech Republic). The nanocatalysts were measured by the X-ray powder diffraction (XRD) pattern obtained with PW1730 Philips (made in the Netherlands). The X-ray photoelectron spectroscopy (XPS) was conducted on the Bes Tec (USA) using Mg radiation. The thermogravimetric analysis (TGA) curve is recorded by the Shimadzu DTG-60 instrument. The concentrations of the organic dyes were monitored by a UV–Vis spectrophotometer (Agilent Technologies Cary 60; made in the USA) at maximum wavelengths (λ_{max}) of 526, 635, 537, 590, 425, and 592 nm for Fast Red, Blue 15, Red 120, Blue 94, Yellow 160, and Acid Orange 7, respectively. The real textile wastewater, including both orange and red Bemacron SER-DL, was prepared from the Farizad Textile Dying Factory in Varamin, Iran. The BOD and COD in wastewater samples were measured by the Standard Methods COD and BOD Reactor (USA-HACH) by Arman Mohit Pak Iranian Company. The specific surface area of samples was determined with the Brunauer-Emmett-Teller (BET) method using the adsorption-desorption isotherms at 77 K (BEL, Belsorp mini II, Made in Japan).

2.2. Preparation of benzoyl pyridinium chloride as a new RTIL

According to our studies on the synthesis of ionic liquid as a green solvent, the benzoyl pyridinium chloride (as a new type of molecular template) was prepared based on the Menshutkin reaction (Supporting information, Fig. S2).

2.2.1. Preparation of SnO (prepared in the absence of RTIL)

About 1 mmol of SnCl$_2$·H$_2$O was added to the 4 mL NaOH (0.1 M) with stirring under reflux. After 3 h, the residue was filtrated, washed with deionized water and ethanol several times, and dried under reduced pressure conditions [14a].

2.3. Preparation of SnO/[BzPy]Cl

SnCl$_2$·H$_2$O (1 mmol) was added to the stirring solution of NaOH (4 mL, 0.1 M) in benzoyl pyridinium chloride (IL) (4 mmol), and the reaction mixture was stirred under reflux conditions for 3 h. The sediment was filtered out, and the collected solid was washed several times using distilled water and ethanol. Finally, it was dried under a vacuum.

2.4. Preparation of nanocomposite SnO/[BzPy]Cl/Ch

The chitosan and bzpyCl were dried at 80 °C for 24 h in a vacuum oven before its use. Next, 1 mmol of chitosan was dissolved in 10 mmol of bzpyCl at 50 °C for 30 min, producing a clear and viscous solution with a concentration of ∼5 wt% (0.125 g of biomass in 2.2 g of bzpyCl). The SnO/[BzPy]Cl/Ch hybrid material was prepared by adding 0.134 g of SnO/[BzPy]Cl nanoparticle to the solution and continuously stirring for 20 min to homogenize the mixture. Subsequently, the solution was dispersed under ultrasonic waves (∼40 kHz) for 1 h and cooled to room temperature. The nanocomposite was washed with ethanol five times. Next, it was washed five times with deionized (DI) water to remove any remaining ILs, then dried for 10 h at 50 °C.

3. Results and discussion

Our previous study presented the synthesis of novel nanocatalysts and their use in the adsorption and degradation of dyes from wastewater [14]. This research presents synthesizing a hybrid nanocomposite SnO/[BzPy]Cl/Ch as a new and effective nanocomposite for the adsorption and degradation of azo and anthraquinone dyes from aqueous solutions. Additionally, this hybrid nanocomposite proves to be efficient for textile wastewater remediation.

3.1. Characterization of IL

The ionic liquid structures were confirmed using ^{1}H NMR (Fig. S3) and FT-IR spectroscopy (Fig. S4).

3.2. Structural studies of bionanocomposite

Fig. 2a–e presents the FT-IR spectra of different stages of the preparation of nanocomposite, including SnO (prepared in the absence of IL), SnO/[BzPy]Cl (SnO prepared in the presence of IL), pure chitosan, SnO/chitosan (prepared in the absence of IL), and SnO/chitosan (prepared in the presence of IL), respectively. The FT-IR results confirm the formation of SnO. The peaks 526 cm^{-1} and 682 cm^{-1} (Fig. 2b) corresponded to the stretching vibration of the Sn–O and Sn–*O*–Sn band, respectively. However, these peaks are weak for the SnO prepared in the absence of IL (Fig. 2a). In the pure chitosan sample (Fig. 2d), the adsorption bands at 603 and 710 cm^{-1} are indexed to the out-of-plane bending NH. Besides, the stretching bands at about 3640, 2881, 1610, 1417, and 1070 cm^{-1} are attributed to the vibrations of NH and OH, CH, NH, CN, and C–*O*–C bands, respectively. After immobilizing SnO on the chitosan for the synthesis of nanocomposite SnO/chitosan, a small shift in the peak position can be seen compared with pure chitosan, confirming the successful anchoring of SnO on chitosan (Fig. 2c and e).

IR spectroscopy also confirms the presence of benzoyl pyridinium chloride molecules in SnO/[BzPy]Cl and SnO/[BzPy]Cl/Ch samples (Fig. 2b and e). Therefore, the ionic liquid not only serves as a template during the formation of tin oxide but also persists within the nanocomposite network due to the influence of intramolecular interactions, such as hydrogen bonding.

Fig. 3 presents the XRD patterns to identify the phase structures of SnO/[BzPy]Cl and SnO/[BzPy]Cl/Ch. According to Fig. 3a, diffraction signals (eight peaks) at $2\theta = 18°, 29°, 32°, 36°, 47°, 50°, 57°$, and $62°$ are represented by their indices 001, 101, 110, 002, 200, 112, 211, and 202, respectively. These peaks are perfectly matched with the standard pattern for the Romarchite phase of Tin(II) oxide (JCPDS, 6–0395) [15].

Furthermore, the XRD pattern of nanocomposite SnO/[BzPy]Cl/Ch (Fig. 3b) shows a small decrease in intensity with a similar peak pattern in comparison to the XRD pattern of SnO/[BzPy]Cl. Consequently, it can be concluded that SnO has correctly coated with the chitosan and IL. Fig. S5 and S6 illustrate the XRD patterns of SnO (prepared in the absence of IL) with SnO (prepared in the presence of IL), SnO/chitosan (prepared in the absence of IL) with SnO/chitosan (prepared in the presence of IL), respectively. As can be seen, the peak intensity of the catalyst synthesized in the presence of ionic liquid is more than that of the catalyst prepared in the absence of IL (See supporting information).

The SEM images of SnO/[BzPy]Cl and SnO/[BzPy]Cl/Ch are shown in Fig. 4, respectively. The morphology was observed using field emission-SEM. As can be seen, the SnO/[BzPy]Cl nanosheets have a network structure with a high surface area and thickness of 97 nm (Fig. 4a). Here, smaller plates are agglomerated and formed irregular plates. The SnO/[BzPy]Cl/Ch, with a plate shape and size distribution of 39–55 nm, was found to be well distinguishable and mostly agglomerate-free. The SEM results revealed the plate shape of SnO/[BzPy]Cl/Ch nanocomposites consisting of hierarchical roughened rose flower-like morphology. The interactions between chitosan and SnO via functional groups strongly prevent the sheets' agglomeration in the matrix and improve the active surface for catalytic dye removal. The porous chitosan containing holes that the SnO dispersed within the porous chitosan as composite and the energy-dispersive x-ray spectroscopy (EDX) spectra proved the presence of Sn, C, H, and O.

The EDX analysis of nanocomposite SnO/chitosan was performed to confirm SnO immobilization on chitosan/[BzPy]Cl. The results demonstrated the presence of N, C, O, and Sn atoms in the modified nanocomposite (Fig. 5).

In this study, an XPS spectrum was prepared to gain insight into the oxidation states of tin in SnO/[BzPy]Cl/Ch. Fig. 6a confirms the presence of constituted elements (O 1s, C 1s, and Sn 3d). Also, according to Fig. 6b, the Sn 3d spectrum exhibited spin-orbit doublet
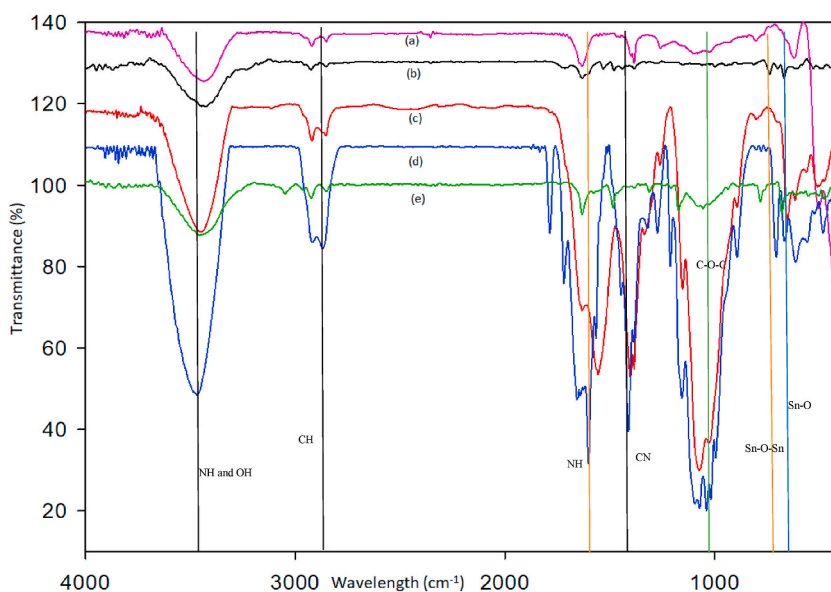

Fig. 2. FTIR spectra of (a) SnO (prepared in absence of IL), (b) SnO/[BzPy]Cl, (c) SnO/chitosan (prepared in absence of IL), (d) pure chitosan, and (e) SnO/[BzPy]Cl/Ch.
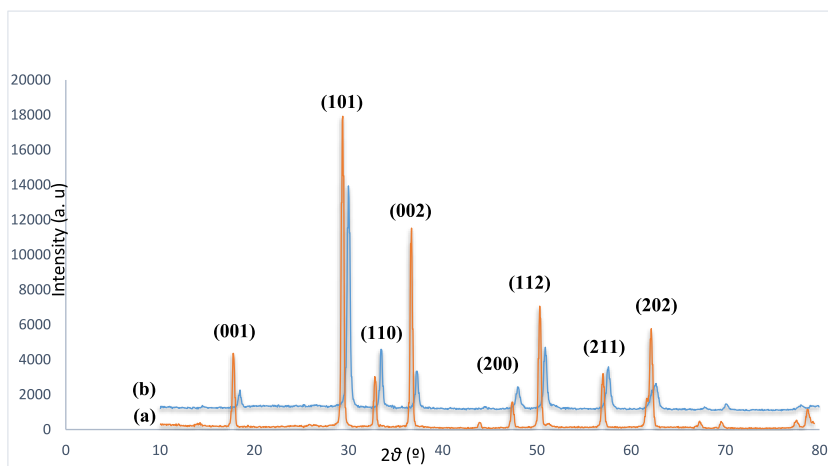
Fig. 3. XRD pattern of (a) SnO/[BzPy]Cl, and (b) SnO/[BzPy]Cl/Ch.

peaks at $\simeq$485 eV (Sn^{2+} 3d$_{5/2}$) and $\simeq$493.5 eV (Sn^{2+} 3d$_{3/2}$).

The N$_2$ adsorption-desorption isotherm was evaluated for SnO/[BzPy]Cl/Ch nanocatalyst. The BET analysis displayed that this nanocomposite belongs to the isotherm type **V** (Fig. 7). The data for the total pore volumes (V$_{total}$) of pure chitosan and the nano-composite are 0.010181 and 0.008124 cm^3/g, respectively. Furthermore, the results for the BET specific surface area (S$_{BET}$) of pure chitosan [16] and the nanocomposite are 1.7461 and 0.96247 m^2/g, respectively. The results show that the surface area and pore volume were decreased by anchoring SnO on the chitosan.

Thermogravimetric analysis (TGA) of the nanocomposite SnO/[BzPy]Cl/Ch revealed significant weight losses between 100 °C and 500 °C (Fig. 8). The first weight loss at around 100 °C was attributed to the evaporation of moisture and intermolecular water from the composite. The second weight loss observed between 100 and 250 °C was directly related to the decomposition of ionic liquid frag-ments. Subsequently, a third weight loss occurred at 250–350 °C, indicating the complete decomposition of chitosan. At higher temperatures (350–500 °C), the decomposition of SnO was observed. As evident from these results, the exceptional thermal stability of SnO/[BzPy]Cl/Ch suggests its promising applicability in high-temperature devices.

Fig. 9 shows the diffused reflectance spectra (DRS) of SnO/[BzPy]Cl and SnO/[BzPy]Cl/Ch. After anchoring SnO onto the chitosan/IL, the bandgap of SnO/[BzPy]Cl, which was originally 3.9 eV due to modification of the structure, was reduced and changed to 3.3 eV.

The calibration curves in Fig. 10 represent the relationship between the amount of absorbance (nm) and concentration (ppm) for different concentrations of six dyes by UV-VIS spectrophotometer. The results obtained from adsorption and photodegradation ex-periments demonstrate the exceptional performance of the SnO/[BzPy]Cl/Ch nanocomposite.

4. Adsorption and photodegradation studies for azo and anthraquinone dyes

The adsorption and degradation performance of various azo and anthraquinone dyes were compared using SnO/[BzPy]Cl nano-particles, chitosan, and SnO/[BzPy]Cl/Ch nanocomposites. The results demonstrated that the SnO/[BzPy]Cl/Ch nanocomposite exhibited superior performance and had a more significant impact compared to the other catalysts. Different parameters were studied on A7, FR, R120, B15, Y160, and B94 dyes removal. Before adding the photocatalyst, sodium hydroxide or hydrochloric acid was added to adjust the acidity of the dye solution. During the dye removal process, the amount of photocatalyst (0.005–0.05 g), dye solution concentration (5–40 mgL^{-1}, 50 mL), contact time (15–150 min), and pH value (2–10) were studied.

4.1. Optimization of solution pH for the removal of dyes

As illustrated in Fig. 11a, the effect of the pH in the range of 2–10 on the adsorption and photodegradation of six azo and anthraquinone dyes was examined. Next, this data was used to determine the surface charge degree of the SnO/[BzPy]C,l/Ch and dye molecules. The data analysis revealed that the maximum removal of dye occurred under acidic conditions at pH = 3 for the A7, FR, and R120 and pH = 4 for the B15, Y160, and B94. Therefore, dye removal was significantly enhanced at pH = 3 and 4. An explanation for this result is that under the acidic condition, the surface charge of the nanocomposite was completely positive. As a result, it led to better electrostatic interaction between a positive surface of nanocomposite and dyes. Hence, the best photodegradation performance was obtained under acidic conditions.

In this respect, sulfonate (–SO$_3$–) groups of dyes are easily dissociated and add to the negative charges in the aquatic environment. Under the acidic condition, the surface charge of the nanocomposite was completely positive, thereby leading to better electrostatic interaction between a positive surface of the nanocomposite and anionic sulfonic groups of the dyes. As the pH of the system decreases, the number of positively charged sites increases, thereby increasing the number of binding sites for anionic dye molecules. The de-protonation of the surface groups in high pH ranges results in the electrostatic repulsion between the anionic dye and negatively
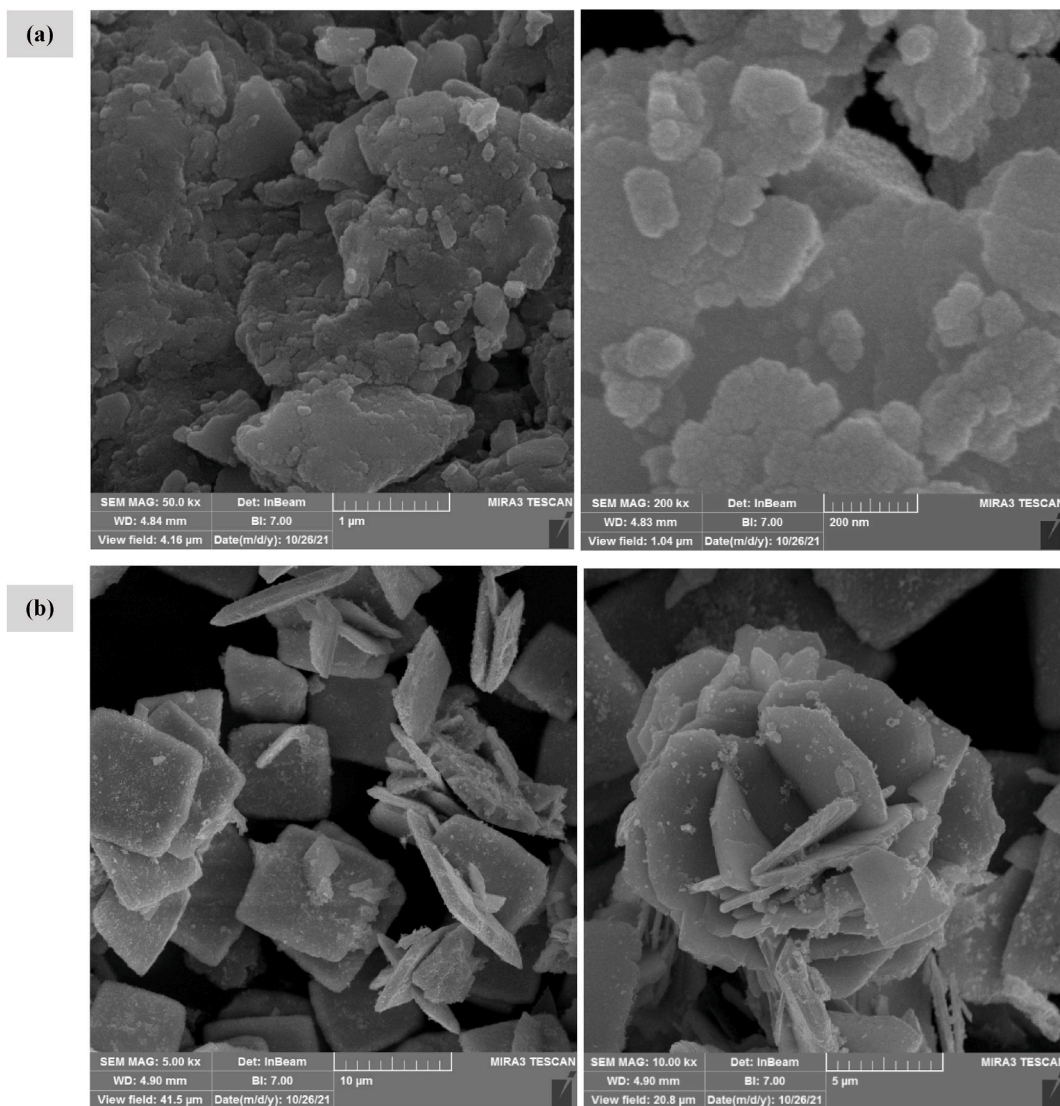
Fig. 4. SEM images of SnO/[BzPy]Cl (a), and nanocomposite SnO/[BzPy]Cl/Ch (b).

charged sites. Therefore, the optimum pH for removing these dyes is between 3 and 4.

5. Optimization of the amount of photocatalyst for the removal of dyes

Fig. 11b presents the experimental results of investigating the effect of the photocatalyst content on the removal of A7, FR, B15, Y160, B94, and R120. It was observed that by increasing the amount of photocatalyst from 2 to 12 and 14 mg, the maximum dye removal was obtained for dyes A7, FR, and B15, and Y160, B94, and R120, respectively. Consequently, by increasing the catalyst dosage, the specific surface area and available active sites for the dye removal were increased. Furthermore, when the catalyst's weight exceeded the mentioned amounts, it appeared that the percentage of dye removal remained unchanged.

6. Contact time studies on adsorption and photodegradation of dyes

Fig. 12a presents the results of the influence of time on the removal of the dyes A7, FR, B15, Y160, B94, and R120. The removal percentage of A7 (96.22 %), FR (97.87 %), B15 (97.20 %), Y160 (97.36 %), B94 (95.76 %), and R120 (97.07 %) were increased up to 105, 90, 120, 90, 105, and 105 min, respectively. Hence, as the contact time increased, the dye removal also increased. This result can be attributed to the enhanced accessibility of numerous active sites on the photocatalyst. However, after exceeding 120 min, the photodegradation percentage remained constant, suggesting the saturation of available active sites.

This outcome can be described in terms of kinetic rate. First, more active sites are exposed as the reaction progresses, leading to
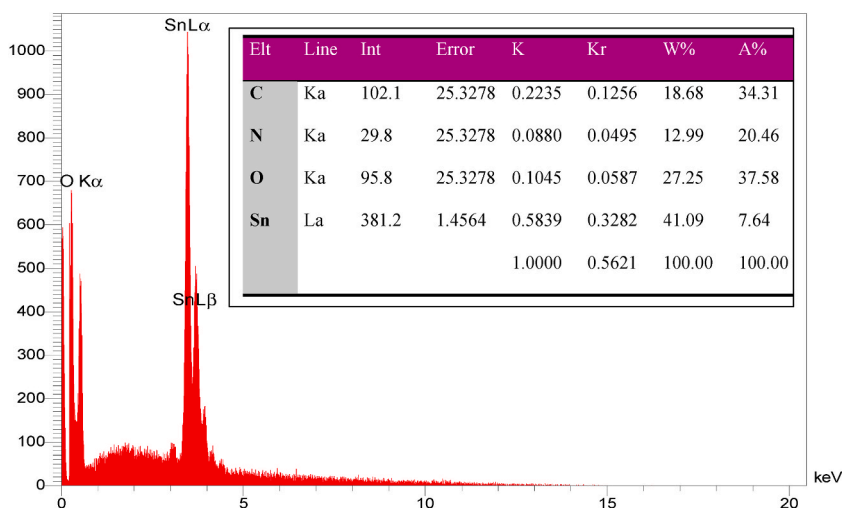
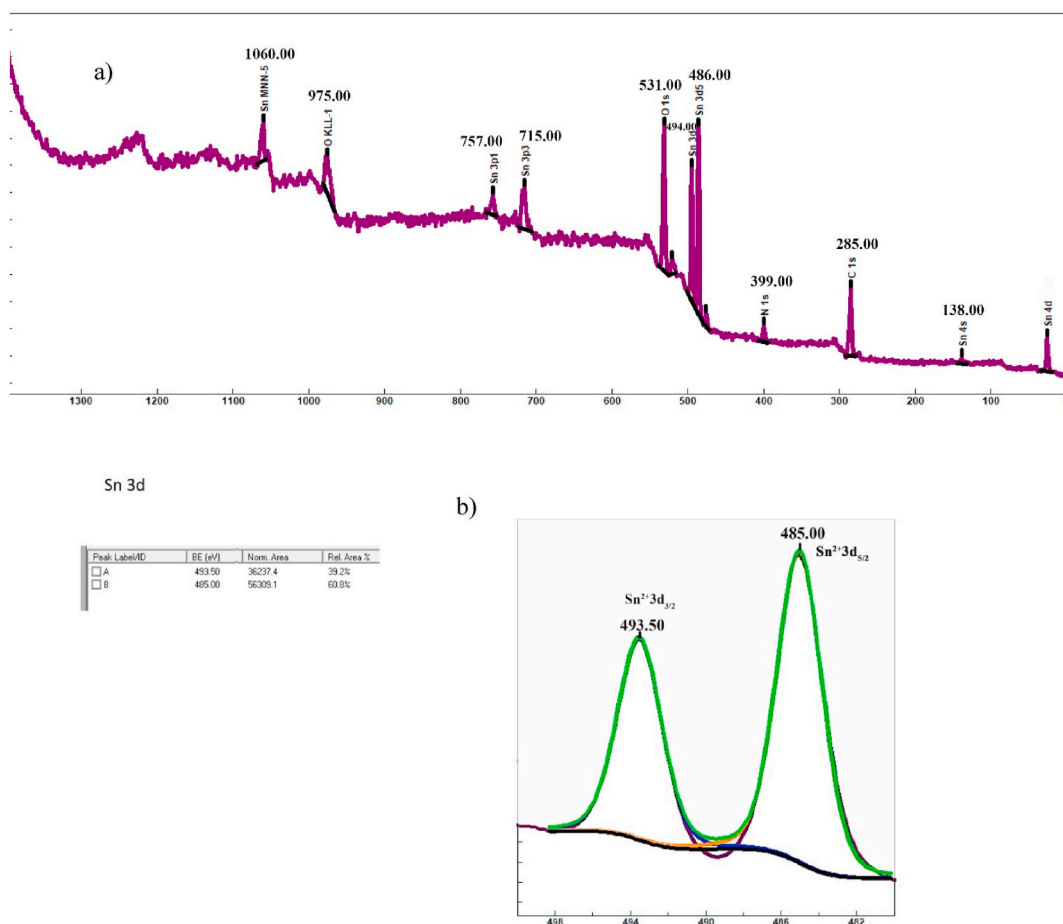**Fig. 5.** EDX spectrum of nanocomposite SnO/[BzPy]Cl/Ch.

Fig. 6. XPS spectra of SnO/[BzPy]Cl/Ch with the full survey (a), Sn (3d) (b).

more effective dye removal. Nevertheless, once these active sites are occupied, further increases in reaction time do not result in additional removal. This result indicates that the reaction has reached equilibrium, and no further significant changes occur in the photodegradation percentage.
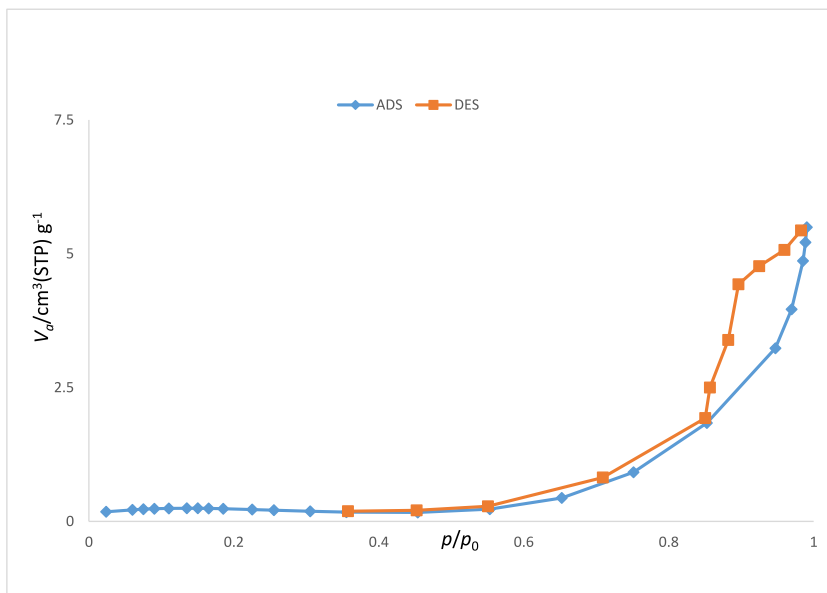
Fig. 7. N_2 adsorption-desorption of nanocomposite SnO/[BzPy]Cl/Ch.
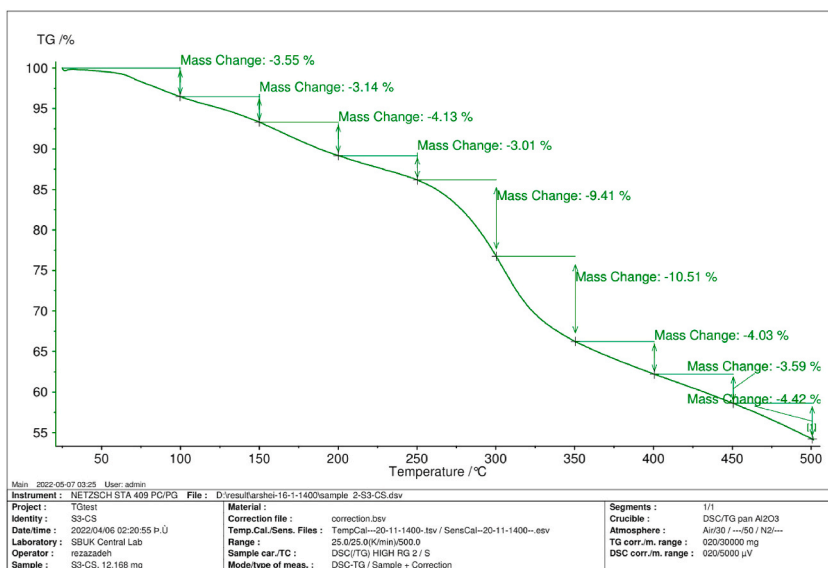

Fig. 8. TGA of nanocomposite SnO/[BzPy]Cl/Ch.

7. Effect of dye concentrations on adsorption and photodegradation of dyes

Fig. 12b shows the results of various dye concentrations, as another important parameter on adsorption and photodegradation of dyes, in the range of 5–80 ppm in the presence of the prepared photocatalyst. Based on the results, the adsorption sites and reactive species became saturated, leading to a decrease in their occupancy and a subsequent reduction in dye removal.

Table 1 presents the best conditions in terms of pH, dye concentration, contact time, and photocatalyst mass for the adsorption and photodegradation of six different dyes with nanocomposite SnO/[BzPy]Cl/Ch.

Based on the obtained optimized conditions, we compared the adsorption and photodegradation of dyes in the presence of SnO, chitosan, and SnO/[BzPy]Cl/Ch under UV and visible light. The results have shown that the best performance was in the presence of nanocomposite SnO/[BzPy]Cl/Ch under UV light (Table 2.).
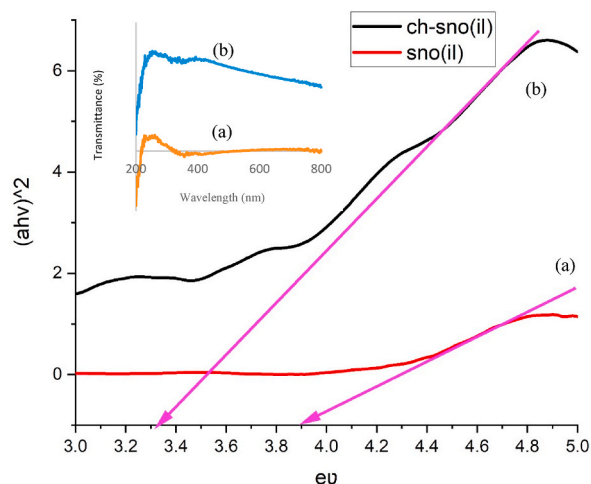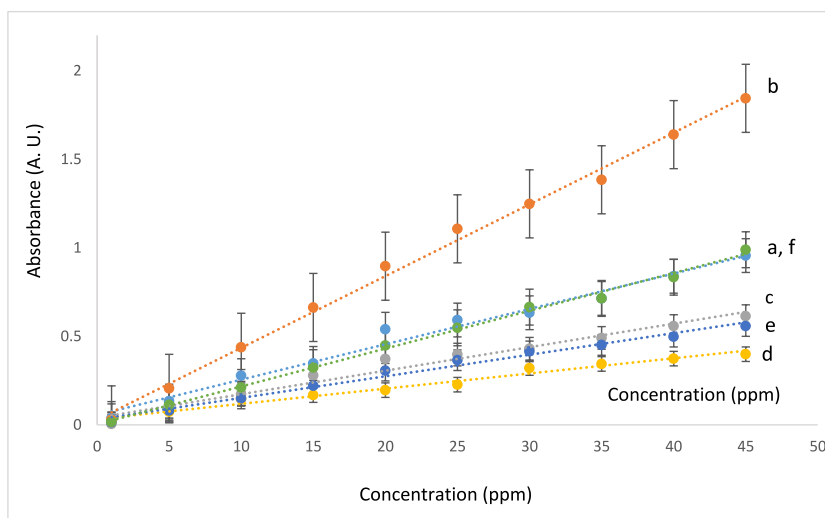
Fig. 9. DRS analysis of (a) SnO/[BzPy]Cl and (b) SnO/[BzPy]Cl/Ch.

(a)	y = 0.02x + 0.0558	(b)	y = 0.0405x + 0.0298	(c)	y = 0.0133x + 0.0402
	$R^2 = 0.9834$		$R^2 = 0.9956$		$R^2 = 0.9716$
(d)	y = 0.0086x + 0.0331	(e)	y = 0.0122x + 0.0304	(f)	y = 0.0214x + 0.0034
	$R^2 = 0.9779$		$R^2 = 0.9866$		$R^2 = 0.9962$

Fig. 10. Calibration curves for (a) A7, (b) FR, (c) B15, (d) Y160, (e) B94, and (f) R120.

8. Effect of temperature on adsorption and photodegradation of dyes

The effect of temperature on the removal rate of Fast Red dye was investigated within a range of 298–300 K. However, no significant change in the removal efficiency was observed. These results indicate that the removal process, whether through adsorption or photodegradation, remained unaffected by variations in temperature within the investigated range. The optimal temperature for removing dyes by the nanocomposite is 25 °C.

9. Dye removal kinetics

For a better comparison of the parameters, the pseudo-first-order and pseudo-second-order models were used to study the dye adsorption kinetics. The pseudo-first-order kinetic model can be integrated in terms of the solid capacity for sorption analysis. Accordingly, and based on equation **a**, the first-order rate constants were calculated:
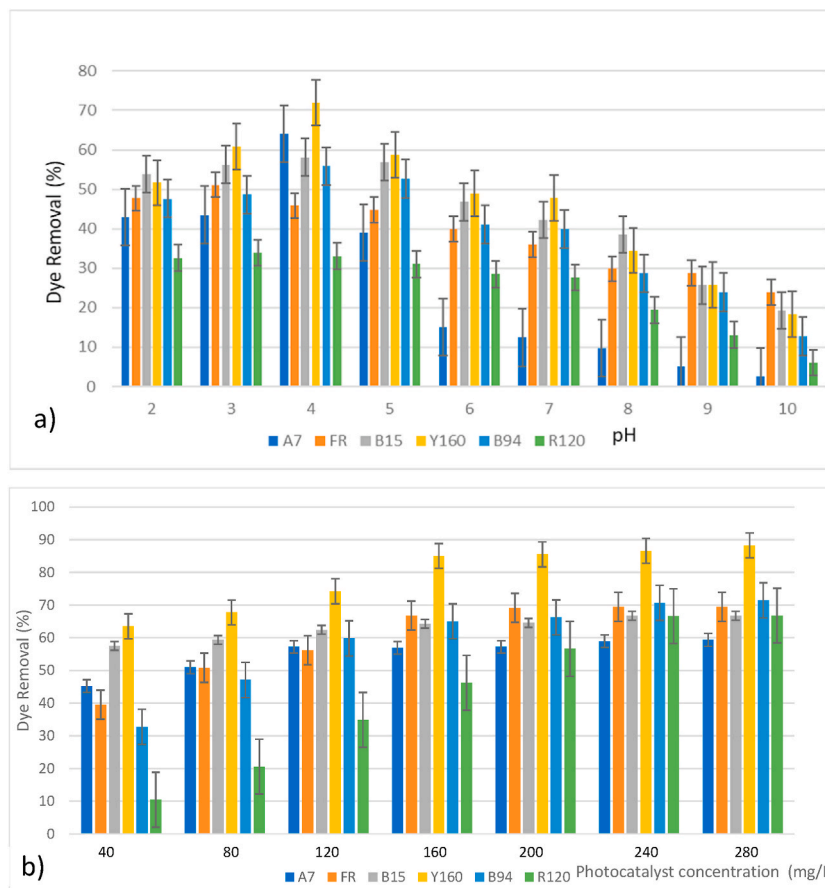
Fig. 11. a) Effect of solution pH value on photodegradation of dyes. b) Effect of photocatalyst concentration on adsorption and photodegradation of dyes.

$$\ln(q_e\text{-}q_t) = \ln q_e\text{-}k_1 t \tag{a}$$

where q_t and q_e are the amounts adsorbed (mol g^{-1}) of dyes at time t (s) and equilibrium, respectively, and k_1 is the pseudo-first-order rate constant (min^{-1}). The values of k_1 (adsorption rate constant) of six dyes were determined according to the plot of ln (q_e-q_t) against t (Fig. 13a). Furthermore, the data of q_e, R^2, and k_1 are given in Table 3.

Eq. (b) presents the pseudo-second-order kinetic model. This equation depends upon the solid adsorption capacity. The k_2 is the equilibrium rate constant of pseudo-second-order (g/mg min). The q_t and q_e are the amounts of dye adsorbed (mg/g) at time t (min) and equilibrium, respectively.

$$\frac{t}{q_t} = \frac{1}{k_2 q_{eq}^2} + \frac{t}{q_{eq}} \tag{b}$$

As shown in Fig. 13b, linear plotting t/q_t against t was used to investigate the applicability of this model. The obtained result is given in Table 3.

Based on the obtained R^2 values (0.9930, 0.9903, 0.9954, 0.9934, 0.9845, and 0.9473), the pseudo-second-order model has a higher R^2 than the pseudo-first-order model for the removal of dyes by nanocomposite SnO/chitosan.

10. Decolorization of real textile wastewater sample

This project examined the application of nanocomposite SnO/chitosan to efficient adsorption and photodegradation of dye from real textile wastewater. To this end, the sample of real textile wastewater was initially filtered by a 0.45 mm membrane filter to remove the debris and suspended particles. Then, a standard solution (20 mg/L) was prepared by dissolving the Fast Red dye in textile wastewater. Subsequently, with the optimal conditions in hand for removing Fast Red dye, adsorption and photodegradation of nanocomposite were measured for a standard solution (textile wastewater containing Fast Red dye). Because of the matrix effect, the tests were performed through the standard addition method, and the final concentrations of the target species after removal with the recommended procedure were determined. The calibration curve of textile wastewater containing Fast Red dye (λ_{max} = 526 nm) is
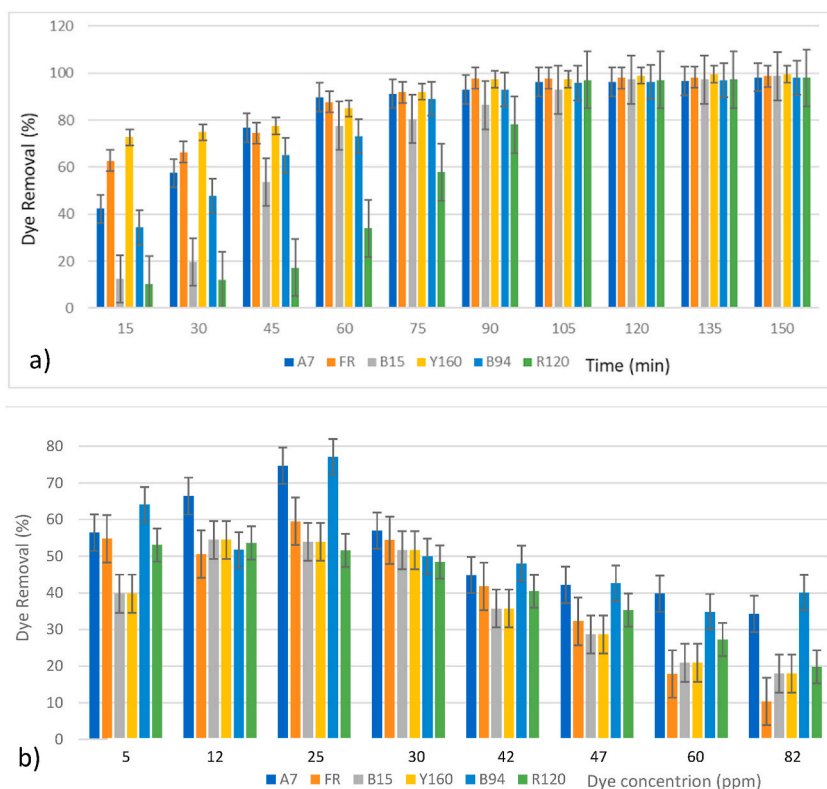
Fig. 12. a) Effect of time on adsorption and photodegradation of dyes. b) Effect of dye concentration on adsorption and photodegradation of dyes.

Table 1
The optimized experiment data for the adsorption and photodegradation of dyes.

Dye	pH	Dye concentration (ppm)	Contact time (min)	Photocatalyst concentration (mg/L)
A7	3	24	105	280
Blue15	4	10	90	240
Blue94	4	20	120	280
Fast red	3	20	90	240
Red120	3	12	105	240
Yellow160	4	11	105	280

Table 2
The comparison results in the performance of different catalysts under light.

Dye	Cat.	Visible	UV	Dye	Cat.	Visible	UV
A7	SnO/[BzPy]Cl	10 %	24 %	Yellow160	SnO/[BzPy]Cl	8 %	20 %
	chitosan	22 %	41 %		chitosan	20 %	45 %
	SnO/[BzPy]Cl/Ch	49 %	95 %		SnO/[BzPy]Cl/Ch	44 %	95 %
Fast red	SnO/[BzPy]Cl	16 %	25 %	Blue94	SnO/[BzPy]Cl	11 %	20 %
	chitosan	19 %	40 %		chitosan	28 %	41 %
	SnO/[BzPy]Cl/Ch	47 %	95 %		SnO/[BzPy]Cl/Ch	47 %	94 %
Blue15	SnO/[BzPy]Cl	16 %	23 %	Red120	SnO/[BzPy]Cl	16 %	23 %
	chitosan	23 %	42 %		chitosan	24 %	44 %
	SnO/[BzPy]Cl/Ch	49 %	94 %		SnO/[BzPy]Cl/Ch	48 %	92 %

depicted in Fig. 14. The results show that the initial and final concentrations were 20 and 0.84 mg/L, respectively, and the removal percentage was about 95.8 %.

11. The BOD and COD reduction analysis

In this study, The degradability of an actual wastewater sample was assessed, along with the examination of chemical oxygen
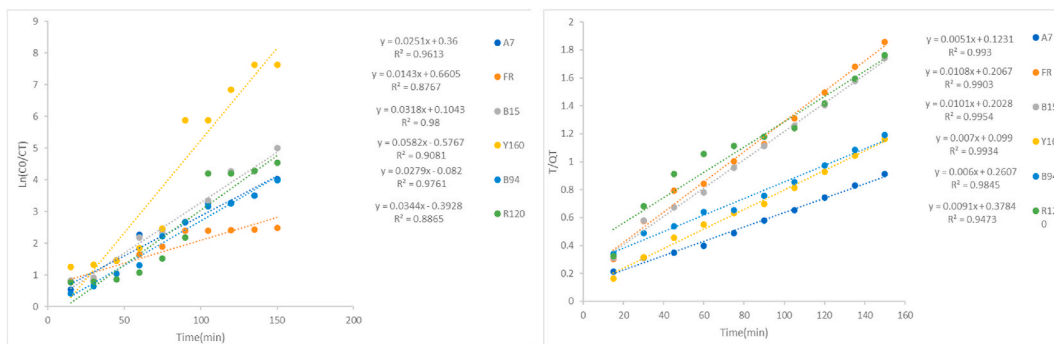
Fig. 13. a) Kinetics plot (pseudo-first-order model) for the adsorption of dyes by SnO/[BzPy]Cl/Ch. b) Kinetics plot (pseudo-second-order model) for the adsorption of dyes by SnO/[BzPy]Cl/Ch.

Table 3
Kinetics constants for the adsorption of dyes by nanocomposite SnO/[BzPy]Cl/Ch.

Kinetics model	Kinetics constants	A7	FR	B15	Y160	B94	R120
Experimental results	$q_{e,exp}$ (mg/g)	164.58	80.792	86.125	129.25	126	80.042
Pseudo – first –	$q_{e,cal}$ (mg/g)	1.433	1.936	1.158	1.78	1.085	1.481
order model	K_1 (min^{-1})	0.0251	0.0143	0.0318	0.0582	0.0279	0.0344
	R^2	0.9613	0.8767	0.98	0.9081	0.9761	0.8865
Pseudo –	$q_{e,cal}$ (mg/g)	196.078	92.593	99.01	142.875	166.667	109.89
second –	K_2 (g/min.mg)	0.0002113	0.0005643	0.000503	0.0004948	0.0001381	0.0002188
order model	R^2	0.9930	0.9903	0.9954	0.9934	0.9845	0.9473

demand (COD) and biological oxygen demand (BOD).

The initial COD concentration of 1910 mg/L decreased to 86 mg/L, indicating a significant reduction. Similarly, the initial BOD concentration of 810 mg/L gradually decreased to 159 mg/L. It is noteworthy that the analysis of BOD and COD was conducted by Arman Mohit Pak, an Iranian company. The adsorbent's performance was evaluated based on the acceptable limits for irrigation (200 mg/L) and agricultural uses (100 mg/L). The results demonstrate that the adsorbent performed exceptionally well, and the treated effluent is suitable for reuse. During the adsorption and photodegradation processes, it is possible that the organic portions of the dye molecules were destroyed, decomposed, or even adsorbed, contributing to the effective treatment.

In the next step, the removal of Fast Red dye from a real textile wastewater sample (95.8 %) was compared with that of synthetic dye solutions (95 %) in the presence of SnO/[BzPy]Cl/Ch catalyst. The results demonstrate the superior performance of the catalyst and, importantly, the presence of no matrix effect on the removal efficiency.

12. Mechanism for removing dye

In heterogeneous photocatalysis systems, the adsorption of dye molecules onto the catalyst surface and photodegradation through photocatalytic reactions occur simultaneously under irradiation. The adsorption of dye serves as a precursor step that facilitates efficient photocatalytic degradation. By concentrating dye molecules on the catalyst surface, adsorption enhances the proximity and contact between the dye and the reactive sites where photocatalytic reactions take place. The adsorbed dye molecules are well-
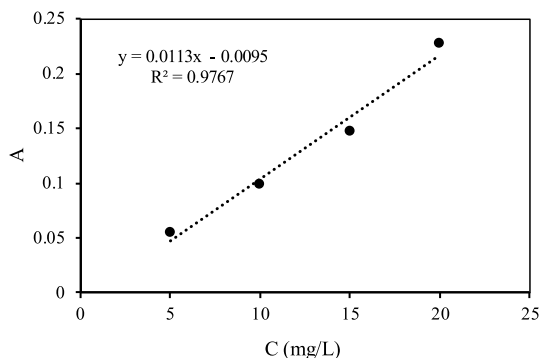

Fig. 14. Calibration curve of wastewater containing fast red dye (λ_{max} = 526 nm).

positioned to undergo oxidation or reduction by photogenerated electrons and holes (Fig. 15).

The process of adsorption takes place through a range of interactions, encompassing hydrogen bonding, electrostatic attractions, and metal coordination. These findings suggest the occurrence of electrostatic attractions, π-π stacking, and hydrogen bonding interactions between the charged IL, chitosan, and negatively charged sulfonate groups of the Fast Red, Blue 15, Red120, Blue 94, Yellow 160, and Acid Orange 7 dyes. Initially, the dye molecules were absorbed by the charged IL and porous chitosan, subsequently forming complexes with the SnO semiconductor and undergoing a subsequent photodegradation process.

13. Recyclability of the bionanocomposite

The regeneration and recyclability of the nanocomposite are crucial factors in water treatment. After the dye removal reaction, the SnO/[BzPy]Cl/Ch nanocomposite was collected through centrifugation and underwent a series of washing steps. First, it was washed with a 1 % acetic acid solution, followed by multiple rinses using distilled water and ethanol. Afterward, the retrieved SnO/[BzPy]Cl/Ch nanocomposite was oven-dried at 50 °C for 5 h. This regenerated nanocomposite was then employed again under optimal conditions for dye removal. The obtained result demonstrates that the nanocomposite exhibited good catalytic activity, allowing for its reuse for at least three cycles (Fig. 16). It is worth noting that the removal percentage after three cycles remained above 72 %.

14. Conclusion

In conclusion, the SnO/[BzPy]Cl nanoparticles and nanocomposite SnO/[BzPy]Cl/Ch were prepared in the presence of benzoyl pyridinium chloride ionic liquid. Based on the obtained experimental results, among different prepared catalysts, the synthesized bionanocomposite SnO/[BzPy]Cl/Ch has the best performance because of improving the band gap values of the catalyst. The SEM images showed the sheet morphology of SnO. Also, after being supported by chitosan and IL, it displayed a layered flower-like structure due to the orientation of the hydrogen bonding effect. The photodegradation and adsorption process depends on the nanocomposite amount, dye concentration, contact time, and solution pH. Followed by achieving the optimal conditions, the efficiency of the novel bionanocomposite in decolorizing real textile wastewater samples was tested, and it demonstrated outstanding performance.

The observed results show a considerable reduction in the BOD and COD values using the prepared photocatalyst. Moreover, different isotherm data and adsorption kinetics models were investigated. Several characterization spectroscopy techniques were used to determine the structures of different catalysts.

Author Statement

On behalf of my co-authors, I certify that all authors have seen and approved the final version of the submitted manuscript. We warrant that the article is the original work, has not received prior publication, and is not under consideration for publication elsewhere.
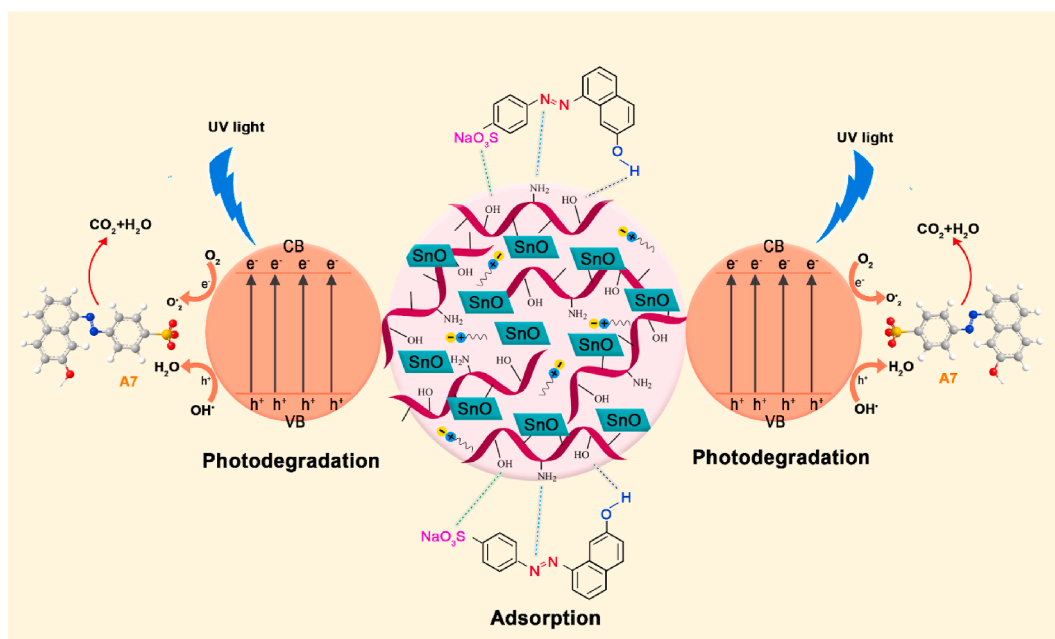

Fig. 15. Plausible adsorption and degradation mechanism for SnO/[BzPy]Cl/Ch.
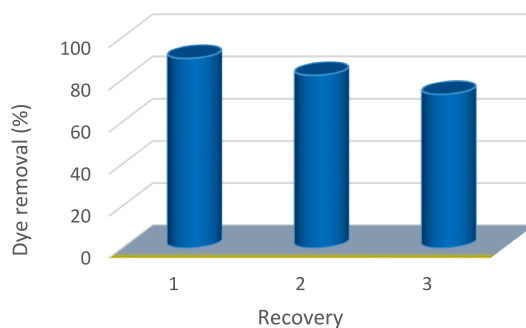
Fig. 16. The reusability of nanocomposite SnO/[BzPy]Cl/Ch for fast red dye removal. (For interpretation of the references to color in this figure legend, the reader is referred to the Web version of this article.)

Data availability

Data will be made available on request.

CRediT authorship contribution statement

Mohammad Hossein Arshia: Writing – original draft, Methodology, Funding acquisition, Data curation. **Ashraf S. Shahvelayati:** Writing – review & editing, Supervision, Project administration. **Shabnam Sheshmani:** Writing – review & editing, Investigation, Formal analysis. **Leila Hajiaghababaei:** Writing – review & editing, Investigation, Formal analysis. **Mohammad Reza Allahgholi Ghasri:** Writing – review & editing.

Declaration of competing interest

The authors declare that they have no known competing financial interests or personal relationships that could have appeared to influence the work reported in this paper.

Acknowledgments

Appendix A. Supplementary data

Supplementary data to this article can be found online at https://doi.org/10.1016/j.heliyon.2024.e24771.

References

[1] (a) U. Habiba, T.C. Joo, T.A. Siddique, A. Salleh, B.C. Ang, A.M. Afifi, Effect of degree of deacetylation of chitosan on adsorption capacity and reusability of chitosan/polyvinyl alcohol/TiO2 nano composite, Int. J. Biol. Macromol. 104 (2017) 1133–1142, https://doi.org/10.1016/j.ijbiomac.2017.07.007;
(b) D. Arikal, A. Kallingal, Photocatalytic degradation of azo and anthraquinone dye using TiO2/MgO nanocomposite immobilized chitosan hydrogels, Environ. Technol. 42 (2021) 2278–2291, https://doi.org/10.1080/09593330.2019.1701094;
(c) A.S. Abdulhameed, A.H. Jawad, A.T. Mohammad, Synthesis of chitosan-ethylene glycol diglycidyl ether/TiO2 nanoparticles for adsorption of reactive orange 16 dye using a response surface methodology approach, Bioresour. Technol. 293 (2019) 122071–122076, https://doi.org/10.1016/j.biortech.2019.122071;
(d) S. Naskar, S. Sharma, K. Kuotsu, Chitosan-based nanoparticles: an overview of biomedical applications and its preparation, J. Drug Deliv. Sci. Technol. 49 (2019) 66–81, https://doi.org/10.1016/j.jddst.2018.10.022;
(e) Y. Zheng, J. Monty, R.J. Linhardt, Polysaccharide-based nanocomposites and their applications, Carbohydr. Res. 405 (2015) 23–32, https://doi.org/10.1016/j.carres.2014.07.016.
[2] a) K. Nomura, H. Ohta, H. Takagi, A. Kamiya, T. Hirano, H. Hosono, Room-temperature fabrication of transparent flexible thin-film transistors using amorphous oxide semiconductors, Nature 432 (2004) 488–492, https://doi.org/10.1038/nature03090;
b) E. Fortunato, P. Barquinha, R. Martins, Oxide semiconductor thin-film transistors: a review of recent advances, Adv. Mater. 24 (2012) 2945–2986, https://doi.org/10.1002/adma.201103228;
c) K. Ellmer, Past achievements and future challengesin the development of optically transparent electrodes, Nat. Photonics 6 (2012) 809–817, https://doi.org/10.1038/nphoton.2012.282;
d) L. Petti, N. Münzenrieder, C. Vogt, H. Faber, L. Büthe, G. Cantarella, F. Bottacchi, T.D. Anthopoulos, G. Tröster, Metal oxide semiconductor thin-film transistors for flexible electronics, Appl. Phys. Rev. 3 (2016) 021303, https://doi.org/10.1063/1.4953034.
[3] M. Batzill, U. Diebold, The surface and materials science of tin oxide, Progress in surface 79 (2005) 47–154, https://doi.org/10.1016/j.progsurf.2005.09.002.

[4] A. Odani, Nimberger, A. Markovsky, B.E. Sominski, E. Levi, V.G. Kumar, M. Motiei, A. Gedanken, P. Dan, D. Aurbach, Development and testing of nanomaterials for rechargeable lithium batteries, J. Power Sources 119 (2003) 517–521, https://doi.org/10.1016/S0378-7753(03)00276-3.

[5] Z. Han, N. Guo, F. Li, W. Zhang, H. Zhao, Y. Qian, Solvothermal preparation and morphological evolution of stannous oxide powders, Mater. Lett. 48 (2001) 99–103, https://doi.org/10.1016/S0167-577X(00)00286-X.

[6] M.T. Greiner, L. Chai, M.G. Helander, W.M. Tang, Z.H. Lu, Transition metal oxide work functions: the influence of cation oxidation state and oxygen vacancies, Adv. Funct. Mater. 22 (2012) 4557–4568, https://doi.org/10.1002/adfm.201200615.

[7] H. Fan, S.A. Reid, Phase transformations in pulsed laser deposited nanocrystalline tin oxide thin films, Chem. Mater. 15 (2003) 564–567, https://doi.org/10.1021/cm0208509.

[8] a) M. Singh, M. Goyal, K. Devlal, Size and shape effects on the band gap of semiconductor compound nanomaterials, J. Taibah Univ. Sci. 12 (2018) 470–475, https://doi.org/10.1080/16583655.2018.1473946;
b) Y. Duan, C.D. Stinespring, B. Chorpening, Electronic structures, bonding configurations, and band-gap-opening properties of graphene binding with low-concentration fluorine, ChemistryOpen 4 (2015) 642–650, https://doi.org/10.1002/open.201500074.

[9] (a) T.J. Trivedi, K.S. Rao, A. Kumar, Facile preparation of agarose–chitosan hybrid materials and nanocomposite ionogels using an ionic liquid via dissolution, regeneration and sol–gel transition, Green Chem. 16 (2014) 320–330, https://doi.org/10.1039/C3GC41317A;
(b) V. Arumugam, K.G. Moodley, A. Dass, R.M. Gengan, D. Ali, S. Alarifi, M. Chandrasekaran, Y. Gao, Ionic liquid covered iron-oxide magnetic nanoparticles decorated zeolite nanocomposite for excellent catalytic reduction and degradation of environmental toxic organic pollutants and dyes, J. Mol. Liq. 342 (2021) 117492, https://doi.org/10.1016/j.molliq.2021.117492.

[10] (a) Y. Huang, G. Ruan, Y. Ruan, W. Zhang, X. Li, F. Du, C. Hu, J. Li, Hypercrosslinked porous polymers hybridized with graphene oxide for water treatment: dye adsorption and degradation, RSC Adv. 8 (2018) 13417–13422, https://doi.org/10.1039/c8ra01620h;
(b) J. Guo, S. Yuan, W. Jiang, H. Yue, Z. Cui, B. Liang, Adsorption and photocatalytic degradation behaviors of rhodamine dyes on surface-fluorinated TiO 2 under visible irradiation, RSC Adv. 6 (2016) 4090–4100, https://doi.org/10.1039/C5RA14379A;
(c) F.P. Van der Zee, S. Villaverde, Combined anaerobic–aerobic treatment of azo dyes a short review of bioreactor, studies Water Res 39 (2005) 1425–1440, https://doi.org/10.1016/j.watres.2005.03.007.

[11] (a) S. Natarajan, H.C. Bajaj, R.J. Tayade, Recent advances based on the synergetic effect of adsorption for removal of dyes from waste water using photocatalytic process, J. Environ. Sci. 65 (2018) 201–222, https://doi.org/10.1016/j.jes.2017.03.011;
(b) K. Golka, S. Kopps, Z.W. Myslak, Carcinogenicity of azo colorants: influence of solubility and bioavailability, Toxicol. Lett. 151 (2004) 203–210, https://doi.org/10.1016/j.toxlet.2003.11.016.

[12] (a) Y. Dong, B. Lu, S. Zang, J. Zhao, X. Wang, Q. Cai, Removal of methylene blue from coloured effluents by adsorption onto SBA-15, J. Chem. Technol. Biotechnol. 86 (2011) 616–619, https://doi.org/10.1002/jctb.2559;
(b) J.K. Kang, J.A. Park, J.H. Kim, C.G. Lee, S.B. Kim, Surface functionalization of mesoporous silica MCM-41 with 3-aminopropyltrimethoxysilane for dye removal: kinetic, equilibrium, and thermodynamic studies, Desalination Water Treat. 57 (2016) 7066–7707, https://doi.org/10.1080/19443994.2015.1014856.

[13] (a) A.H. Jawad, B.H. Hameed, A.S. Abdulhameed, Synthesis of biohybrid magnetic chitosan-polyvinyl alcohol/MgO nanocomposite blend for remazol brilliant blue R dye adsorption: solo and collective parametric optimization, Environ. Chem. Eng 9 (2022) 105166–105179, https://doi.org/10.1007/s00289-022-04294-z;
(b) J. Chen, B. Liu, X. Gao, D. Xu, A review of the interfacial characteristics of polymer nanocomposites containing carbon nanotubes, RSC Adv. 8 (2018) 28048–28085, https://doi.org/10.1039/C8RA04205E.

[14] (a) A.S. Shahvelayati, S. Sheshmani, M. Siminghad, Preparation and characterization of SnO nanoflowers with controllable thicknesses using imidazolium-based ionic liquids as green media: visible light photocatalytic degradation of Acid Blue 19, Mater. Chem. Phys. 278 (2022) 125442–125450, https://doi.org/10.1016/j.matchemphys.2021.125442;
(b) M. Siminghad, S. Sheshmani, A.S. Shahvelayati, Application, optimisation and kinetic studies of SnO micro-square in photoinduced decolourisation of Acid Orange 7 and Acid Orange 10 under visible light irradiation, Int. J. Environ. Anal. Chem. 101 (2021) 473–481, https://doi.org/10.1080/03067319.2019.1668931;
(c) M. Siminghad, A.S. Shahvelayati, S. Sheshmani, R. Ahmadi, Ionic liquid-assisted synthesis, characterization and photocatalytic properties of SnO microflowers with nanosheet subunits, J. Nanoanalysis 6 (2019) 228–236, https://doi.org/10.22034/JNA.2019.669635;
(d) S. Alibakhshi, A.S. Shahvelayati, S. Sheshmani, M. Ranjbar, S. Souzangarzadeh, Design, synthesis, and characterization of a novel Zn(II) 2 phenyl benzimidazole framework for the removal of organic dyes, Sci. Rep. 12 (2022) 12431, https://doi.org/10.1038/s41598-022-16753-8.

[15] H. Uchiyama, H. Ohgi, H. Imai, Selective preparation of SnO2 and SnO crystals with controlled morphologies in an aqueous solution system, Cryst. Growth Des. 6 (2006) 2186–2190, https://doi.org/10.1021/cg060328p.

[16] N.T. Nguyen, N.T.V.A. Nguyen, Nguyen, in situ synthesis and characterization of ZnO/chitosan nanocomposite as an adsorbent for removal of Congo red from aqueous solution, Adv. Polym. Technol. (2020) 3892694–3892713, https://doi.org/10.1155/2020/3892694.